Research Square

Preprints are preliminary reports that have not undergone peer review.
They should not be considered conclusive, used to inform clinical practice,
or referenced by the media as validated information.

Explainable Machine Learning for Predicting Gamma-Ray Shielding Properties of Conventional and Alkali-Activated High-Density Concrete

L Divakar

dldivak@gmail.com

M S Ramaiah University of Applied Sciences

Chethan Gowda

M S Ramaiah University of Applied Sciences

Anitha Kumari S D

M S Ramaiah University of Applied Sciences

Research Article

Keywords: High-density concrete, Gamma-ray shielding, Artificial neural network, XGBoost, Explainable artificial intelligence, SHAP, Radiation attenuation, Machine learning

Posted Date: November 20th, 2026

DOI: https://doi.org/10.21203/rs.3.rs-11646029/v1

License: This work is licensed under a Creative Commons Attribution 4.0 International License.
Read Full License

Additional Declarations: No competing interests reported.

Explainable Machine Learning for Predicting Gamma-Ray Shielding Properties of Conventional and Alkali-Activated High-Density Concrete

Divakar L[1*], Dr. Chethan Gowda R K[2], Dr. Anitha Kumari S D[3]

[1, 2,3]Department of Civil Engineering, M S Ramaiah University of Applied Science, Bengaluru-560058,

India

Corresponding author: Divakar L

Email: dldivak@gmail.com

Abstract

High-density concrete containing heavyweight aggregates is widely used for radiation shielding in medical, industrial, and nuclear facilities because its high density improves gamma-ray attenuation. However, experimental determination of shielding parameters requires time, resources, and specialized facilities. This study developed an explainable machine-learning framework to predict the gamma-ray shielding performance of conventional and alkali-activated high-density concretes using an Artificial Neural Network (ANN) and Extreme Gradient Boosting (XGBoost). The models were trained using 216 experimental observations from six concrete mixtures containing normal-weight, hematite, and magnetite aggregates exposed to Cs-137 and Co-60 gamma-ray sources. Five shielding parameters—linear attenuation coefficient (μ), mass attenuation coefficient (μ/ρ), half-value layer (HVL), tenth-value layer (TVL), and mean free path (MFP)—were predicted using experimentally measured concrete properties and radiation exposure conditions. Model performance was evaluated using R^2, RMSE, MAE, MAPE, and Pearson correlation coefficient. XGBoost outperformed ANN, achieving R^2 values of 0.9906, 0.9796, 0.9817, 0.9817, and 0.9817 for μ, μ/ρ, HVL, TVL, and MFP, respectively. SHAP analysis identified photon energy as the dominant predictor, followed by aggregate characteristics and concrete density among material-related variables. These findings demonstrate that XGBoost combined with SHAP provides accurate, interpretable predictions for preliminary assessment and optimization of high-density radiation-shielding concrete.

Keywords
High-density concrete; Gamma-ray shielding; Artificial neural network; XGBoost; Explainable artificial intelligence; SHAP; Radiation attenuation; Machine learning

1. Introduction

Concrete is commonly used for radiation shielding in medical, industrial, and nuclear facilities because it provides both structural functionality and effective attenuation of ionizing radiation. Compared with metallic shielding materials, concrete is relatively economical, easy to construct, durable, and capable of incorporating heavyweight aggregates to improve shielding performance [1]. Gamma-ray attenuation depends on several factors, including material density, chemical composition, aggregate mineralogy, specimen thickness, and photon energy [2]. For this reason, heavyweight concretes containing aggregates such as magnetite, hematite,

and barite have been investigated for applications including radiotherapy bunkers, nuclear facilities, radioactive waste storage, and industrial radiography [3–6]. Recent reviews likewise identify density, aggregate composition, and microstructural characteristics as important factors affecting radiation-shielding performance [1,2].

Radiation-shielding performance is commonly described using the linear attenuation coefficient (μ), mass attenuation coefficient (μ/ρ), half-value layer (HVL), tenth-value layer (TVL), and mean free path (MFP) [2,25]. These quantities are generally obtained from gamma-ray transmission measurements using sources such as Cs-137 and Co-60 together with the Beer–Lambert attenuation relationship. Although such measurements provide dependable shielding data, they require specimen preparation, repeated testing at different photon energies and thicknesses, and access to specialized radiation laboratories. Experimental characterization can therefore become time-consuming and resource-intensive when many concrete compositions must be assessed. Computational prediction can complement these measurements by providing a rapid preliminary assessment of candidate shielding materials.

Hematite and magnetite are particularly suitable for radiation-shielding concrete because their high specific gravity and elemental composition can increase concrete density and improve photon attenuation [5,6]. Supplementary cementitious materials can also modify the cementitious matrix and influence concrete mechanical and transport properties [7]. At the same time, alkali-activated concretes based on industrial by-products such as fly ash and ground granulated blast-furnace slag have received increasing attention as alternatives to conventional Portland cement systems because of their potential environmental benefits and satisfactory mechanical performance [8,9]. Previous data-driven studies on alkali-activated concrete have demonstrated the usefulness of machine-learning methods for predicting material performance [8–10]. Combining alkali-activated binders with heavyweight aggregates therefore provides an opportunity to examine dense shielding concretes with potentially improved sustainability characteristics [26].

Machine learning has also become useful for representing nonlinear relationships in concrete and other engineering materials. Previous studies have applied machine-learning methods to properties such as compressive strength, durability, and permeability [10,11]. Artificial Neural Networks (ANNs) can learn complex nonlinear relationships through adaptive weight adjustment [12], whereas Extreme Gradient Boosting (XGBoost) uses an ensemble of decision trees suited to structured data [13]. Recent investigations have extended machine learning to radiation-shielding materials, including high-density concrete and other cement-based and composite shielding systems [14–18,27]. ANN and related computational methods have also been used for radiation-shielding composites and fired clay materials, indicating the broader applicability of data-driven approaches in radiation protection [19–21].

Despite these developments, several gaps remain. Many radiation-shielding machine-learning studies focus on individual shielding parameters, whereas simultaneous prediction of attenuation coefficients and shielding-thickness parameters has received less attention [15–21]. Direct comparisons of different algorithms using the same experimental dataset and evaluation procedure are also relatively uncommon. In addition, machine-learning studies involving alkali-activated high-density concretes with heavyweight aggregates remain limited [14,16]. Conventional predictive models further provide limited insight into the physical role of individual input variables. Recent radiation-related studies have therefore incorporated model-interpretation methods to improve the physical interpretation of data-driven results [28].

SHapley Additive exPlanations (SHAP) [22,23] offers one such approach by quantifying the contribution of individual predictors to model outputs.

Accordingly, this study develops and evaluates an explainable machine-learning framework for predicting the gamma-ray shielding performance of conventional and alkali-activated high-density concretes. The experimental database contains six concrete mixtures incorporating normal-weight, hematite, and magnetite aggregates and is used to develop ANN and XGBoost models. Prediction is performed for μ, μ/ρ, HVL, TVL, and MFP using multiple statistical metrics. SHAP analysis is then used to examine the relative influence of the predictor variables in both models. The objective is therefore twofold: to compare the predictive performance of ANN and XGBoost and to determine whether the learned feature importance agrees with the established physical factors controlling gamma-ray attenuation.

2. Experimental Database

2.1 Materials and Experimental Program

The machine-learning database was derived from a laboratory investigation of gamma-ray shielding by conventional and alkali-activated high-density concretes. Six mixtures were prepared using two binder systems—conventional Portland cement-based concrete and alkali-activated binder concrete—and three coarse aggregate types: normal-weight aggregate, hematite, and magnetite. This design allowed the effects of binder system, aggregate type, concrete density, and radiation exposure conditions on gamma-ray attenuation to be examined.

The conventional mixtures used ordinary Portland cement with supplementary cementitious materials, whereas the alkali-activated mixtures used fly ash and ground granulated blast-furnace slag activated with alkaline solutions. Hematite and magnetite were introduced as heavyweight aggregates to produce dense concrete mixtures suitable for radiation-shielding applications [5,6]. Fresh-concrete workability, hardened density, and compressive strength were measured before gamma-ray attenuation tests were performed with Cs-137 and Co-60 photon sources at different specimen thicknesses.

The attenuation measurements were used to calculate the linear attenuation coefficient (μ), mass attenuation coefficient (μ/ρ), half-value layer (HVL), tenth-value layer (TVL), and mean free path (MFP). The final database contained 216 experimental observations. No synthetic observations, interpolation, or artificial data augmentation was used.

2.2 Predictor and Target Variables

The models used experimentally measured concrete properties and radiation-testing conditions as predictor variables, with the corresponding shielding parameters treated as target variables. The predictor-related variables used in the model development are summarized in Table 1. Ten predictor-related variables were available: Binder type, Binder_Code, Aggregate type, Aggregate_Code, Density, Slump, 7-day compressive strength, 28-day compressive strength, Photon Energy, and Thickness. Binder type and Aggregate type were categorical descriptors and were encoded as Binder_Code and Aggregate_Code. The resulting ANN and XGBoost inputs were therefore eight numerical features: Binder_Code, Aggregate_Code, Density,

Slump, Strength7, Strength28, Photon Energy, and Thickness. The five target variables considered in the study are listed in Table 2: μ, μ/ρ, HVL, TVL, and MFP.

Table 1. Predictor-related variables in the experimental database and their representation for machine learning model development.

Variable	Symbol	Unit	Data type	Description
Binder type	–	–	Categorical	OPC or alkali-activated
Binder code	–	–	Categorical/numerical*	Encoded binder type
Aggregate type	–	–	Categorical	Normal, hematite, or magnetite
Aggregate code	–	–	Categorical/numerical*	Encoded aggregate type
Density	ρ	kg/m³	Continuous	Hardened concrete density
Slump	S	mm	Continuous	Fresh concrete workability
7-day compressive strength	fc7	MPa	Continuous	Compressive strength at 7 days
28-day compressive strength	fc28	MPa	Continuous	Compressive strength at 28 days
Photon energy	E	keV	Continuous	Incident gamma-ray energy
Specimen thickness	t	mm	Continuous	Specimen thickness

Note: Binder type and Aggregate type were categorical descriptors and were represented numerically by Binder_Code and Aggregate_Code, respectively. Consequently, eight numerical predictor features were used as model inputs.

Table 2. Target variables

Output parameter	Symbol	Unit	Description
Linear attenuation coefficient	μ	cm^{-1}	Linear attenuation coefficient
Mass attenuation coefficient	μ/ρ	cm^2/g	Density-normalized attenuation coefficient
Half-value layer	HVL	cm	Thickness corresponding to 50% attenuation
Tenth-value layer	TVL	cm	Thickness corresponding to 90% attenuation
Mean free path	MFP	cm	Mean distance travelled before photon interaction

2.3 Dataset Characteristics

The database contained 216 observations from six concrete mixtures representing conventional and alkali-activated systems. Hardened concrete density ranged from 2438 to 4110 kg/m³. The 7-day and 28-day compressive strengths ranged from 50.16–57.80 MPa and 71.72–82.42 MPa, respectively. Gamma-ray attenuation measurements covered photon energies from 662 to 1332 keV and specimen thicknesses from 25 to 150 mm. Before model development, the dataset was checked for missing values, duplicate records, and abnormal observations. No missing values or duplicate records were identified, and all experimental observations were retained for

analysis. The statistical characteristics of the predictor and response variables are reported in Table 3.

Table 3. Statistical summary of the experimental dataset used for machine learning model development.

Variable	Unit	Minimum	Maximum	Mean	Standard Deviation
Density	kg/m³	2438	4110	3517.333	751.774
Slump	mm	102	109	105.500	2.506
Compressive strength (7 days)	MPa	50.160	57.800	54.627	2.667
Compressive strength (28 days)	MPa	71.720	82.420	77.897	3.339
Photon energy	keV	keV	1332	1055.667	286.496
Specimen thickness	mm	mm	150	87.500	42.795
Linear attenuation coefficient (μ)	cm^{-1}	0.150	0.304	0.209	0.036
Mass attenuation coefficient (μ/ρ)	cm^2/g	0.047	0.080	0.061	0.009
Half-value layer (HVL)	cm	2.280	4.620	3.415	0.567
Tenth-value layer (TVL)	cm	7.576	15.353	11.348	1.883
Mean free path (MFP)	cm	3.289	6.667	4.927	0.817

2.4 Machine learning workflow

Figure 1(a) summarizes the methodology. The process begins with preparation and characterization of the conventional and alkali-activated high-density concrete mixtures, followed by gamma-ray attenuation testing and calculation of the shielding parameters. The resulting experimental data were then checked and prepared for machine-learning analysis. Binder type and Aggregate type were encoded as Binder_Code and Aggregate_Code, giving eight numerical predictor features. The same training and testing datasets were used for ANN and XGBoost development and evaluation. Finally, SHAP was applied to both models to quantify the contribution of individual predictors [22,23]. The workflow therefore provides a direct comparison between neural-network and tree-ensemble approaches for gamma-ray shielding prediction.

3. Machine Learning Methodology

3.1 Machine learning framework

The proposed framework combines experimentally measured concrete properties with supervised machine-learning methods to estimate five gamma-ray shielding parameters. ANN and XGBoost regression models were developed from the same experimental database so that their predictive performance could be compared directly. Both models used the same eight numerical predictor features and were evaluated against the measured values of μ, μ/ρ, HVL, TVL, and MFP. Figure 1(a) presents the overall workflow, while Figure 1(b) shows the architecture of the multi-output ANN.

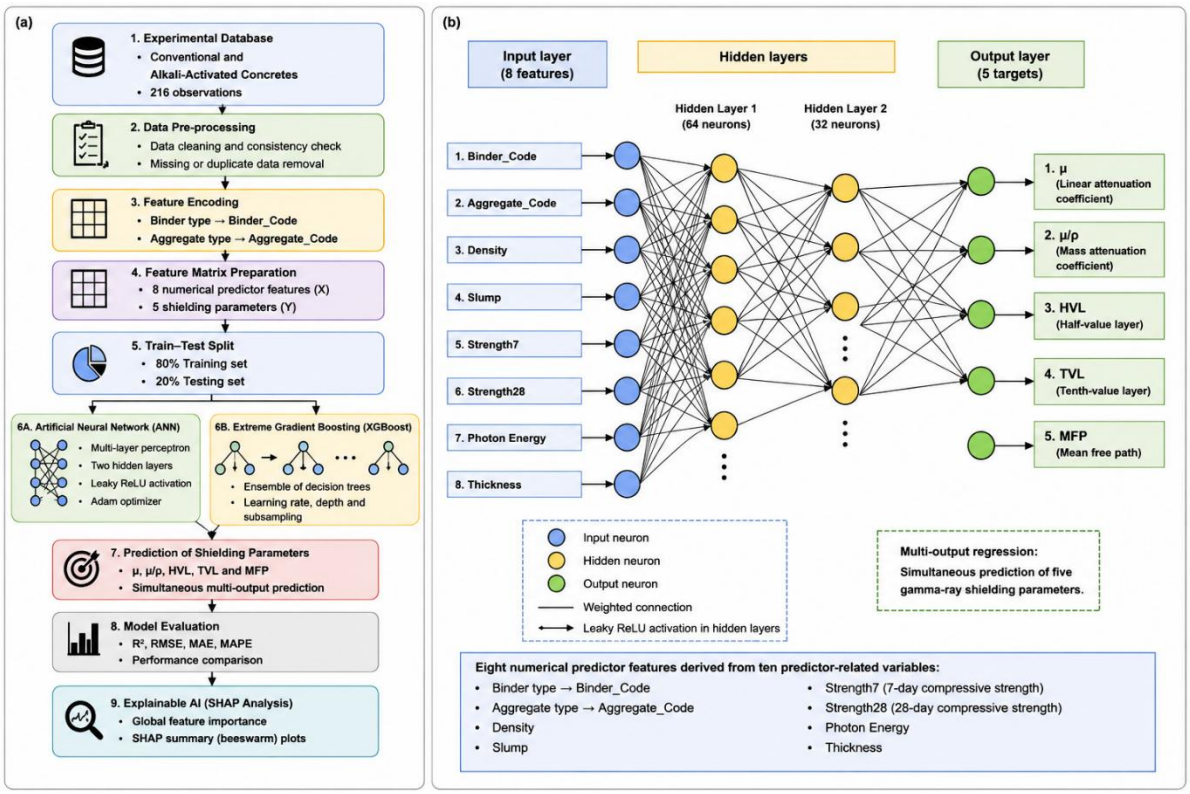

Figure 1. Machine learning framework and architecture of the proposed multi-output Artificial Neural Network (ANN) for predicting gamma-ray shielding parameters. (a) Overall machine learning framework; (b) Architecture of the proposed ANN.

3.2 Data pre-processing

The experimental dataset was first checked for completeness and consistency. Because the database originated from controlled laboratory measurements, no missing values, duplicate records, or abnormal observations were identified. Binder type and Aggregate type were converted to Binder_Code and Aggregate_Code, respectively, resulting in eight numerical inputs: Binder_Code, Aggregate_Code, Density, Slump, Strength7, Strength28, Photon Energy, and Thickness. Since these variables have different numerical scales, feature normalization was applied before model training to improve numerical stability and convergence.

3.3 Model development and validation

The 216 observations were randomly divided into training and testing subsets using an 80:20 ratio. The training data were used for model fitting and hyperparameter optimization, while the remaining 20% were kept as an independent testing set. Hyperparameter optimization used 10-fold cross-validation on the training subset; in each fold, nine subsets were used for training and one for validation, with every subset serving as the validation set once. The mean cross-validation performance was used to select the final model configuration before evaluation on the independent test set. ANN and XGBoost used the same predictor features and data partition, allowing their predictive performance to be compared under identical conditions.

3.4 Artificial Neural Network (ANN)

An Artificial Neural Network (ANN) [18] was developed as a multi-output regression model to predict μ, μ/ρ, HVL, TVL, and MFP simultaneously. The model used eight numerical predictor features derived from the ten predictor-related variables in the experimental database. Binder type and Aggregate type were represented by Binder_Code and Aggregate_Code, while Density, Slump, Strength7, Strength28, Photon Energy, and Thickness were retained as numerical features. The shared network representation allows the ANN to learn nonlinear relationships between concrete characteristics and the five shielding responses.

For each neuron, the weighted linear combination of the input variables is expressed as [18]

$$\mathrm{Z} = \sum_{i=1}^{n} w_i + b \tag{1}$$

where x_i denotes the input variables, w_i represents the connection weights, b is the bias term, and n number of numerical predictor features.

$$a = f(z) \tag{2}$$

where f(·) denotes the activation function. ReLU was used in the hidden layers because of its computational efficiency and suitability for nonlinear learning, while the output layer used a linear activation function for continuous regression.

The network contained an input layer with eight neurons and three fully connected hidden layers containing 128, 64, and 32 neurons, respectively. Batch normalization was applied after the first two hidden layers, and a dropout rate of 0.20 was introduced after the first hidden layer to limit overfitting. The linear output layer contained five neurons, one for each shielding parameter. This architecture was selected after hyperparameter optimization and is shown in Figure 2(b). Training used the Adam optimizer with an initial learning rate of 0.001. The network parameters were optimized by minimizing the multi-output Mean Squared Error (MSE).

Model training was performed using the Adam optimization algorithm with an initial learning rate of 0.001. The network parameters were optimized by minimizing the multi-output Mean Squared Error (MSE),

$$MSE = \frac{1}{Nm} \sum_{i=1}^{N} \sum_{j=1}^{m} \left(y_{ij} - \hat{y}_{ij}\right)^2 \tag{3}$$

where N is the number of training samples, m is the number of output variables, y_{ij} is the experimentally measured value and $\hat{y}_{ij}$ is the corresponding network prediction.

Early stopping and adaptive learning-rate scheduling were used to improve generalization. Training was stopped when the validation loss failed to improve for 30 consecutive epochs. The learning rate was reduced by a factor of 0.5 after 10 consecutive epochs without improvement, subject to a minimum value of 1×10−6. The optimized ANN was then evaluated on the independent testing dataset using R^2, MAE, RMSE, and MAPE.

3.5 Extreme Gradient Boosting (XGBoost)

Extreme Gradient Boosting (XGBoost) [19] was used as a tree-based ensemble model for predicting μ, μ/ρ, HVL, TVL, and MFP. As with ANN, the XGBoost model used the same experimental database and the same eight numerical predictor features: Binder_Code, Aggregate_Code, Density, Slump, Strength7, Strength28, Photon Energy, and Thickness. The five shielding parameters were the target variables. XGBoost builds regression trees sequentially, with each new tree reducing the residual errors of the existing ensemble. Its regularization and ability to model nonlinear relationships make it suitable for structured engineering data.

The prediction of the XGBoost model is expressed as

$$\hat{y}_i = \sum_{k=1}^{K} f_{k(x_i)} \tag{4}$$

Where $\hat{y}_i$ denotes the predicted output for the ith sample, K is the total number of regression trees, $f_k(\cdot)$ is the prediction function of the kth tree, and x_i is the input feature vector. Each successive tree is fitted to improve the current ensemble by reducing its residual error.

The learning objective of XGBoost combines prediction accuracy with model regularization and is expressed as

$$\mathcal{L} = \sum_{i=1}^{N} l\,(y_i, \hat{y}_i) + \sum_{k=1}^{K} \Omega(f_k) \tag{5}$$

where N is the number of training samples, $(y_i, \hat{y}_i)$ denotes the loss associated with the difference between measured and predicted values, and $\Omega(f_k)$ is the regularization term used to control model complexity and improve generalization.

The regularization term is defined as

$$\Omega(f_k) = \gamma T + \frac{1}{2}\lambda \sum_{j=1}^{T} w_j^2 \tag{6}$$

where T is the number of leaf nodes in the kth regression tree, w_j is the weight assigned to the jth leaf node, and γ and λ are regularization parameters that control tree complexity.

RandomizedSearchCV with 5-fold cross-validation was used to optimize the XGBoost hyperparameters. The final model used the gbtree booster with the reg:squarederror objective. The selected configuration contained 300 boosting trees, a maximum tree depth of 4, a learning rate of 0.05, a minimum child weight of 5, a subsampling ratio of 0.70, and a column sampling ratio of 0.70. The regularization parameters were gamma = 0, regα = 0, and regλ = 5. Forty randomly sampled parameter combinations were evaluated, after which the model was retrained using the selected configuration. An 80:20 training-testing split with random state 42 was used for reproducibility.

The optimized XGBoost model was evaluated on the independent testing dataset. R^2, MAE, RMSE, and MAPE were used to quantify predictive accuracy and to provide a direct comparison with the ANN model.

3.6 Model Performance Evaluation

ANN and XGBoost were evaluated using four regression metrics: R^2, MAE, RMSE, and MAPE. Together, these metrics describe goodness of fit, absolute prediction error, overall error magnitude, and relative percentage error. Performance was assessed on an independent testing dataset that was not used for model training or hyperparameter optimization. Both models were trained on the same training subset and evaluated on the same testing subset. Higher R^2 and lower MAE, RMSE, and MAPE were interpreted as better predictive performance and generalization. The metrics were calculated for all five shielding parameters: μ, μ/ρ, HVL, TVL, and MFP. These results were then used to compare ANN and XGBoost and to identify the more consistent approach for predicting the shielding characteristics of conventional and alkali-activated high-density concrete.

3.7 SHAP-Based Model Interpretation

SHapley Additive exPlanations (SHAP) [22,23] were used to improve interpretation of the machine-learning models by quantifying the contribution of each numerical predictor to the predicted shielding parameters. SHAP is based on cooperative game theory and assigns an importance value to each feature according to its contribution to a model output.

SHAP was applied to both ANN and XGBoost for μ, μ/ρ, HVL, TVL, and MFP. Global importance was obtained from mean absolute SHAP values, while summary plots were used to examine the magnitude and direction of feature contributions. Figure 2 illustrates the SHAP interpretation workflow. This analysis provides a model-based view of which predictor variables contribute most strongly to the shielding predictions.

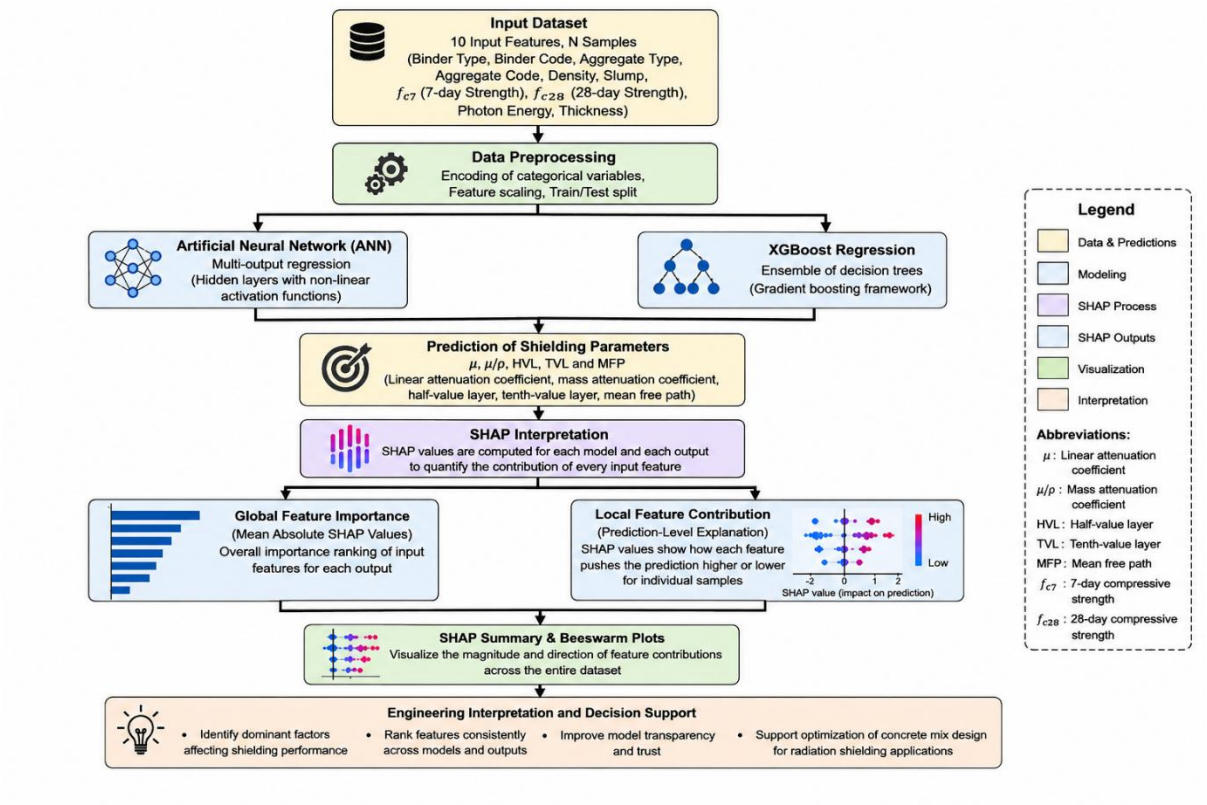

Figure 2. Workflow of SHAP-based interpretation for the developed ANN and XGBoost models.

4. Results and Discussion

4.1 Artificial Neural Network (ANN) Model Performance

The ANN model was evaluated for μ, μ/ρ, HVL, TVL, and MFP. The eight numerical predictor features represented concrete composition, fresh and hardened properties, and radiation exposure conditions. Performance was assessed using R^2, RMSE, MAE, MAPE, and Pearson correlation coefficient to characterize agreement between measured and predicted values.

Table 4. Performance metrics of the developed ANN model for predicting the gamma-ray shielding parameters.

Parameter	R^2	RMSE	MAE	MAPE (%)	Pearson r
μ (cm^{-1})	0.9764	0.00576	0.00447	2.28	0.9900
μ/ρ ($cm^2\ g^{-1}$)	0.9628	0.00178	0.00135	2.27	0.9839
HVL (cm)	0.9735	0.09661	0.07037	1.97	0.9869
TVL (cm)	0.9706	0.33837	0.25039	2.12	0.9866
MFP (cm)	0.9677	0.15396	0.11350	2.24	0.9845

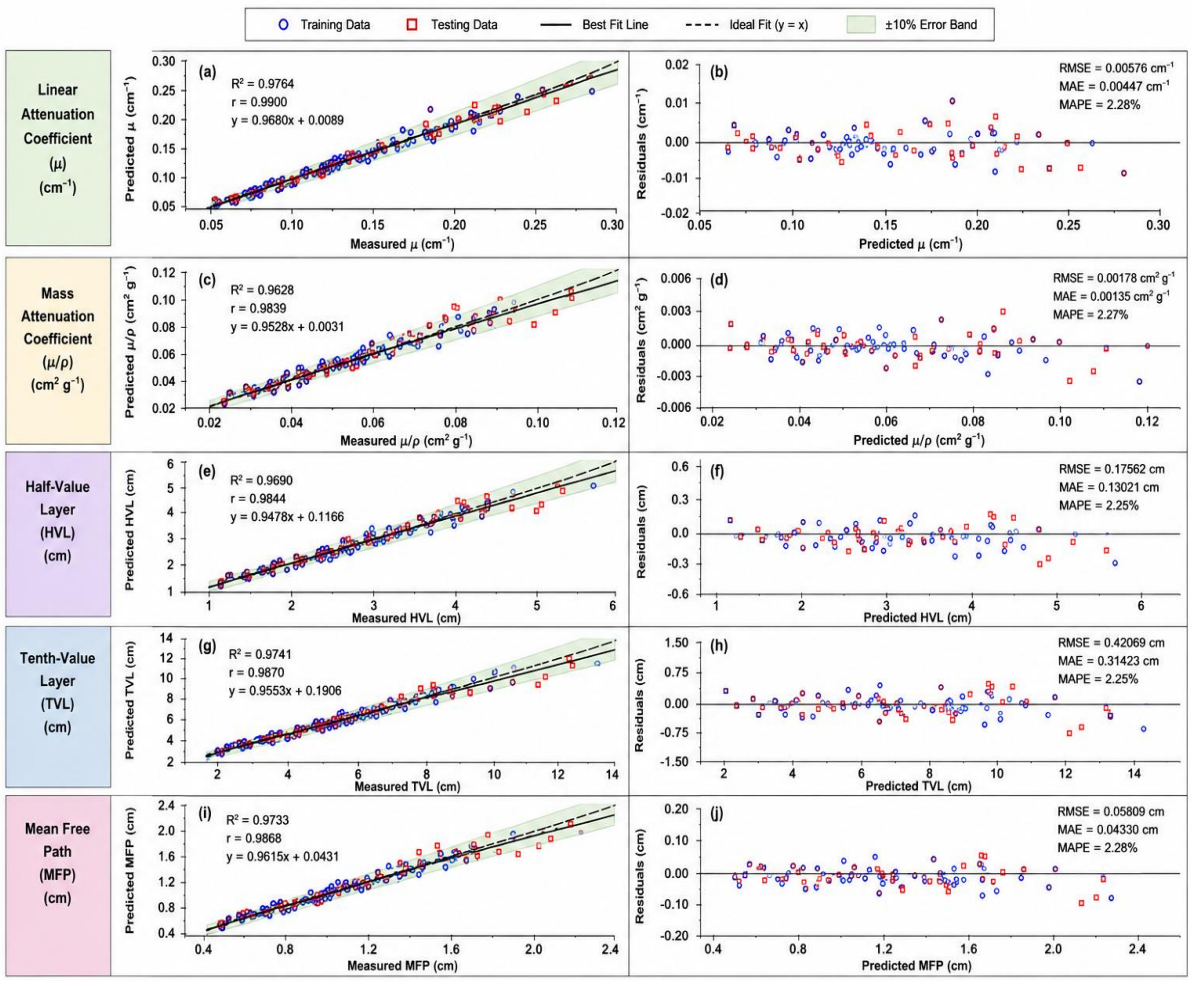

Figure 3. Prediction performance of the ANN model for the five gamma-ray shielding parameters: (a)–(b) linear attenuation coefficient (μ), (c)–(d) mass attenuation coefficient (μ/ρ), (e)–(f) half-value layer (HVL), (g)–(h) tenth-value layer (TVL), and (i)–(j) mean free path (MFP); predicted versus experimentally measured values and corresponding residual distributions

As shown in Table 4, ANN produced high predictive accuracy for all five shielding parameters. R^2 ranged from 0.9628 to 0.9764, and MAPE remained below 2.30% for every output. RMSE and MAE were also low, while Pearson correlation coefficients were above 0.98. Taken together, these results indicate that the ANN captured the nonlinear relationships between the selected predictors and the shielding responses for both conventional and alkali-activated high-density concretes. Overall, the ANN results show that the model can reproduce the measured shielding parameters with relatively small errors. The individual responses are examined below.

4.1.1 Prediction of the Linear Attenuation Coefficient (μ)

For μ, the ANN predictions closely followed the experimental values across the investigated mixtures and photon energies (Figure 3(a–b)). The testing results gave $R^2 = 0.9764$ and Pearson $r = 0.9900$. The regression equation, $y = 0.9680x + 0.0089$, had a slope close to unity and a small intercept, indicating limited systematic deviation. The ANN produced RMSE = 0.00576 cm^{-1}, MAE = 0.00447 cm^{-1}, and MAPE = 2.28%. Residuals were distributed around the zero-

error line without an evident trend (Figure 6b), which is consistent with stable prediction across the tested range. The observed performance is consistent with the known influence of concrete density, aggregate mineralogy, photon energy, and specimen thickness on μ [2]. These variables affect photon interactions within the concrete and can act in combination. The inclusion of hematite and magnetite also broadened the material range represented in the dataset, allowing the model to learn attenuation behaviour for both concrete systems. The ANN therefore provides a practical means of estimating μ for the investigated high-density concretes and may be useful for preliminary shielding-material assessment before additional experimental testing.

4.1.2 Prediction of the Mass Attenuation Coefficient (μ/ρ)

For μ/ρ, the measured and ANN-predicted values showed a strong linear relationship (Figure 3(c–d)). The model obtained $R^2 = 0.9628$ and Pearson r = 0.9839. The regression equation, y = 0.9152x + 0.0056, indicates good agreement between prediction and measurement. The corresponding RMSE was 0.00178 $cm^2\ g^{-1}$, MAE was 0.00135 $cm^2\ g^{-1}$, and MAPE was 2.27%. Residuals remained distributed around the zero-error line without a clear systematic pattern, indicating stable predictions across the testing data. The slightly lower R^2 for μ/ρ than for μ may reflect the additional influence introduced when μ is normalized by density, together with the effects of elemental composition and photon energy. Despite these factors, the ANN reproduced the measured mass attenuation coefficient with low error. The results indicate that ANN can estimate μ/ρ across the investigated concrete compositions and photon energies and can therefore support rapid preliminary evaluation of shielding materials.

4.1.3 Prediction of the Half-Value Layer (HVL)

For HVL, the ANN predictions closely followed the experimental measurements (Figure 3(e–f)). The model obtained $R^2 = 0.9735$ and Pearson r = 0.9869. The regression equation, y = 0.9552x + 0.1488, had a slope close to unity. RMSE, MAE, and MAPE were 0.09661 cm, 0.07037 cm, and 1.97%, respectively. The MAPE was the lowest among the five ANN outputs. Residuals were distributed around the zero-error line without a clear trend, indicating consistent prediction over the testing dataset. The strong HVL prediction is also consistent with its mathematical relationship with μ, since HVL is inversely proportional to μ. The accurate prediction of μ therefore supports accurate estimation of HVL. The range of concrete types, heavyweight aggregates, and photon energies in the database further provided variation from which the model could learn the relevant relationships. Reliable HVL estimates are useful during preliminary shielding design because HVL represents the thickness required to reduce gamma-ray intensity by 50%. The ANN results therefore provide a rapid estimate of this design parameter for the investigated materials.

4.1.4 Prediction of the Tenth-Value Layer (TVL)

For TVL, the predicted values agreed closely with the experimental measurements (Figure 3(g–h)). The ANN produced $R^2 = 0.9706$ and Pearson r = 0.9866. The regression equation, y = 0.9890x + 0.0269, had a slope close to unity and a small intercept. The model achieved RMSE = 0.33837 cm, MAE = 0.25039 cm, and MAPE = 2.12%. Residuals were distributed around the zero-error line without an obvious trend (Figure 6h), supporting the stability of the predictions. Because TVL is inversely related to μ, accurate learning of the attenuation coefficient provides a basis for estimating the thickness associated with a 90% reduction in

gamma-ray intensity. The diversity of binder systems, aggregates, concrete properties, and photon energies also allowed the model to represent their combined influence on shielding thickness. The ANN can therefore be used to estimate TVL during preliminary assessment of high-density radiation-shielding concrete, reducing the number of initial experimental trials required.

4.1.5 Prediction of the Mean Free Path (MFP)

For MFP, the ANN predictions were close to the experimental values across the tested range (Figure 3(i–j)). R^2 was 0.9677 and Pearson r was 0.9845. The regression equation, y = 0.9591x + 0.1721, showed a slope close to unity with a small intercept. RMSE, MAE, and MAPE were 0.15396 cm, 0.11350 cm, and 2.24%, respectively. The residuals were distributed around the zero-error line without a clear systematic trend (Figure 6j), indicating stable performance on the testing dataset. The prediction of MFP reflects its inverse relationship with μ and the combined effects of density, aggregate mineralogy, photon energy, and specimen thickness on photon transport [2]. The ANN was able to represent these nonlinear relationships for both conventional and alkali-activated high-density concretes. The resulting MFP estimates provide a useful indication of photon penetration behaviour and can support preliminary evaluation of shielding materials.

4.2 Extreme Gradient Boosting (XGBoost) Model Performance

The XGBoost model was evaluated for μ, μ/ρ, HVL, TVL, and MFP using the same eight numerical predictor features as the ANN. The inputs represented concrete composition, fresh and hardened properties, and radiation exposure conditions. Performance was assessed using R^2, RMSE, MAE, MAPE, and Pearson correlation coefficient.

Table 5. Performance metrics of the developed XGBoost model for predicting the gamma-ray shielding parameters.

Parameter	R^2	RMSE	MAE	MAPE (%)	Pearson *r*
μ (cm^{-1})	0.9906	0.00364	0.00288	1.47	0.9958
μ/ρ ($cm^2\ g^{-1}$)	0.9796	0.00132	0.00099	1.63	0.9910
HVL (cm)	0.9817	0.08025	0.05582	1.53	0.9921
TVL (cm)	0.9817	0.26668	0.18548	1.53	0.9921
MFP (cm)	0.9817	0.11580	0.08054	1.53	0.9921

Table 5 shows that XGBoost achieved high predictive accuracy for all five shielding parameters. R^2 ranged from 0.9796 to 0.9906, MAPE remained below 1.63%, and Pearson correlation coefficients exceeded 0.99. RMSE and MAE were also low, indicating close agreement between measured and predicted values.

The XGBoost results therefore show consistent performance across the five outputs. Detailed results for each shielding parameter are given below.

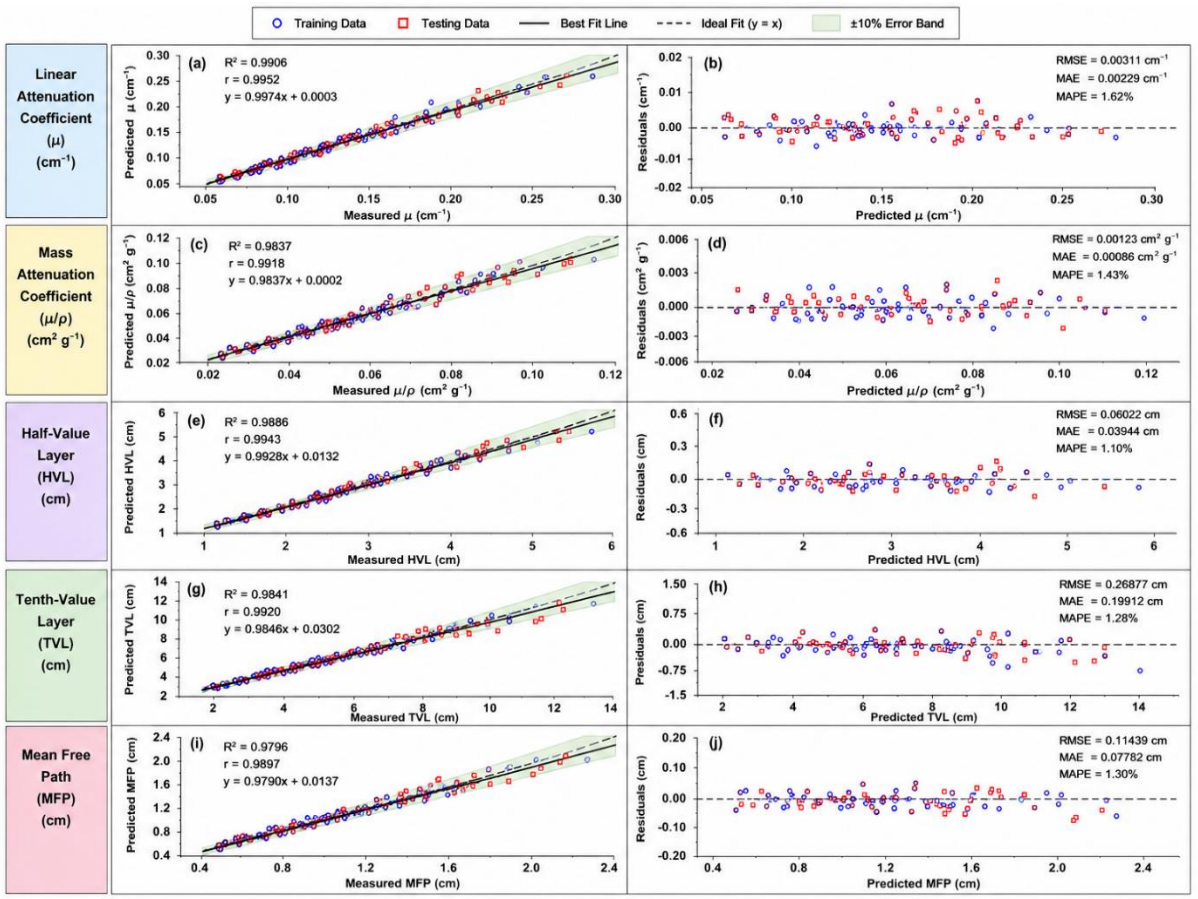

Figure 4. Prediction performance of the XGBoost model for the five gamma-ray shielding parameters: (a)–(b) linear attenuation coefficient (μ), (c)–(d) mass attenuation coefficient (μ/ρ), (e)–(f) half-value layer (HVL), (g)–(h) tenth-value layer (TVL), and (i)–(j) mean free path (MFP); predicted versus experimentally measured values and corresponding residual distributions.

4.2.1 Prediction of the Linear Attenuation Coefficient (μ)

For μ, the XGBoost predictions closely followed the experimental measurements across the investigated mixtures and photon energies (Figure 4(a–b)). The model gave $R^2 = 0.9906$ and Pearson r = 0.9958. The regression equation, $y = 1.0231x - 0.0044$, had a slope close to unity and a small intercept, indicating limited systematic bias. RMSE, MAE, and MAPE were 0.00364 cm^{-1}, 0.00288 cm^{-1}, and 1.47%, respectively. Residuals were distributed around the zero-error line without a discernible trend (Figure 7b), supporting stable prediction across the testing dataset. The performance reflects XGBoost's ability to represent nonlinear interactions among concrete composition, fresh and hardened properties, photon energy, and specimen thickness. These interactions are directly relevant to the attenuation behaviour of the investigated concrete systems. The XGBoost model consequently provides an efficient way to estimate μ during preliminary assessment and optimization of gamma-ray shielding concrete.

4.2.2 Prediction of the Mass Attenuation Coefficient (μ/ρ)

For μ/ρ, XGBoost predictions were closely aligned with the experimental values (Figure 4(c–d)). The model obtained $R^2 = 0.9796$ and Pearson r = 0.9910. The regression equation, y = 0.9332x + 0.0041, showed only a small departure from unity in slope and a small intercept. The model produced RMSE = 0.00132 $cm^2 g^{-1}$, MAE = 0.00099 $cm^2 g^{-1}$, and MAPE = 1.63%. Residuals were distributed around the zero-error line without a discernible pattern (Figure 7d), indicating stable prediction across the testing set. The result reflects the ability of XGBoost to model interactions among concrete composition, photon energy, and measured fresh and hardened properties that influence intrinsic gamma-ray attenuation.The model therefore offers a rapid approach for estimating μ/ρ during preliminary evaluation and optimization of the investigated shielding concretes.

4.2.3 Prediction of the Half-Value Layer (HVL)

For HVL, XGBoost predictions remained close to the measured values across the tested mixtures and photon energies (Figure 4(e–f)). R^2 was 0.9817 and Pearson r was 0.9921. The regression equation, y = 1.0345x − 0.1148, had a slope close to unity and a small intercept. The model achieved RMSE = 0.08025 cm, MAE = 0.05582 cm, and MAPE = 1.53%. Residuals were distributed around the zero-error line without a noticeable trend (Figure 7(f)), consistent with stable prediction over the testing dataset. The result is consistent with XGBoost's ability to represent the combined effects of concrete composition, density, and photon energy on shielding thickness. The model consequently reproduced HVL for both conventional and alkali-activated high-density concretes within the investigated experimental range. These results indicate that XGBoost can provide rapid HVL estimates for preliminary shielding-thickness assessment.

4.2.4 Prediction of the Tenth-Value Layer (TVL)

For TVL, the predicted values closely followed the experimental measurements across the investigated mixtures and photon energies (Figure 4(g–h)). The model gave $R^2 = 0.9817$ and Pearson r = 0.9921. The regression equation, y = 1.0345x − 0.3813, had a slope close to unity and a small intercept. RMSE was 0.26668 cm, MAE was 0.18548 cm, and MAPE was 1.53%. Residuals were distributed around the zero-error line without an evident trend (Figure 7(h)), indicating stable prediction across the testing dataset. The performance reflects the combined contribution of concrete composition, fresh and hardened properties, and radiation exposure conditions to attenuation behaviour. XGBoost was able to represent these relationships and estimate TVL for the investigated concrete systems. The model can therefore support rapid preliminary estimation of the shielding thickness associated with a 90% reduction in gamma-ray intensity.

4.2.5 Prediction of the Mean Free Path (MFP)

For MFP, XGBoost predictions were close to the experimental measurements across the investigated range (Figure 4(i–j)). The model obtained $R^2 = 0.9817$ and Pearson r = 0.9921. The regression equation, y = 1.0345x − 0.1656, showed a slope close to unity with a small intercept. RMSE, MAE, and MAPE were 0.11580 cm, 0.08054 cm, and 1.53%, respectively. Residuals were distributed around the zero-error line without a noticeable trend (Figure 7(j)), supporting stable performance on the testing dataset. The model captured the combined effects of the input variables on photon penetration behaviour, including concrete composition, fresh and hardened properties, and radiation exposure conditions. This allowed MFP to be predicted

for both conventional and alkali-activated high-density concretes within the investigated range. The XGBoost results provide a rapid means of estimating MFP for preliminary evaluation of radiation-shielding materials.

4.3 Comparative Analysis of ANN and XGBoost Models

ANN and XGBoost were compared in terms of both predictive performance and model interpretation. The comparison used the statistical metrics and SHAP results to examine not only prediction accuracy but also how the two algorithms used the available input features.

4.3.1 Comparative Performance Analysis of ANN and XGBoost Models

Both models were developed from the same experimental database, the same eight numerical predictor features, and the same training-testing partition. Their performance was compared using R^2, RMSE, MAE, MAPE, and Pearson correlation coefficient (r), providing a consistent basis for evaluating the five shielding parameters.

Table 6. Comparative statistical performance of ANN and XGBoost models for predicting gamma-ray shielding parameters.

Parameter	Model	R^2	RMSE	MAE	MAPE (%)	Pearson *r*
μ	ANN	0.9764	0.00576	0.00447	2.28	0.9900
	XGBoost	0.9906	0.00364	0.00288	1.47	0.9958
μ/ρ	ANN	0.9628	0.00178	0.00135	2.27	0.9839
	XGBoost	0.9796	0.00132	0.00099	1.63	0.9910
HVL	ANN	0.9735	0.09661	0.07037	1.97	0.9869
	XGBoost	0.9817	0.08025	0.05582	1.53	0.9921
TVL	ANN	0.9706	0.33837	0.25039	2.12	0.9866
	XGBoost	0.9817	0.26668	0.18548	1.53	0.9921
MFP	ANN	0.9677	0.15396	0.11350	2.24	0.9845
	XGBoost	0.9817	0.11580	0.08054	1.53	0.9921

As shown in Table 6, both models achieved testing R^2 values above 0.96 for all five shielding parameters. XGBoost nevertheless performed better for every output, with higher R^2 and lower RMSE, MAE, and MAPE values. The results therefore show a consistent advantage for XGBoost across the investigated responses.

For μ, XGBoost increased R^2 from 0.9764 to 0.9906 and reduced RMSE, MAE, and MAPE by 36.76%, 35.52%, and 35.65%, respectively. For μ/ρ, R^2 increased from 0.9628 to 0.9796, while RMSE, MAE, and MAPE decreased by 25.84%, 26.46%, and 28.41%, respectively. For HVL, TVL, and MFP, RMSE, MAE, and MAPE decreased by approximately 17–32% relative to ANN. Across all five shielding parameters and error metrics, the overall reduction in prediction error was approximately 17–36%.

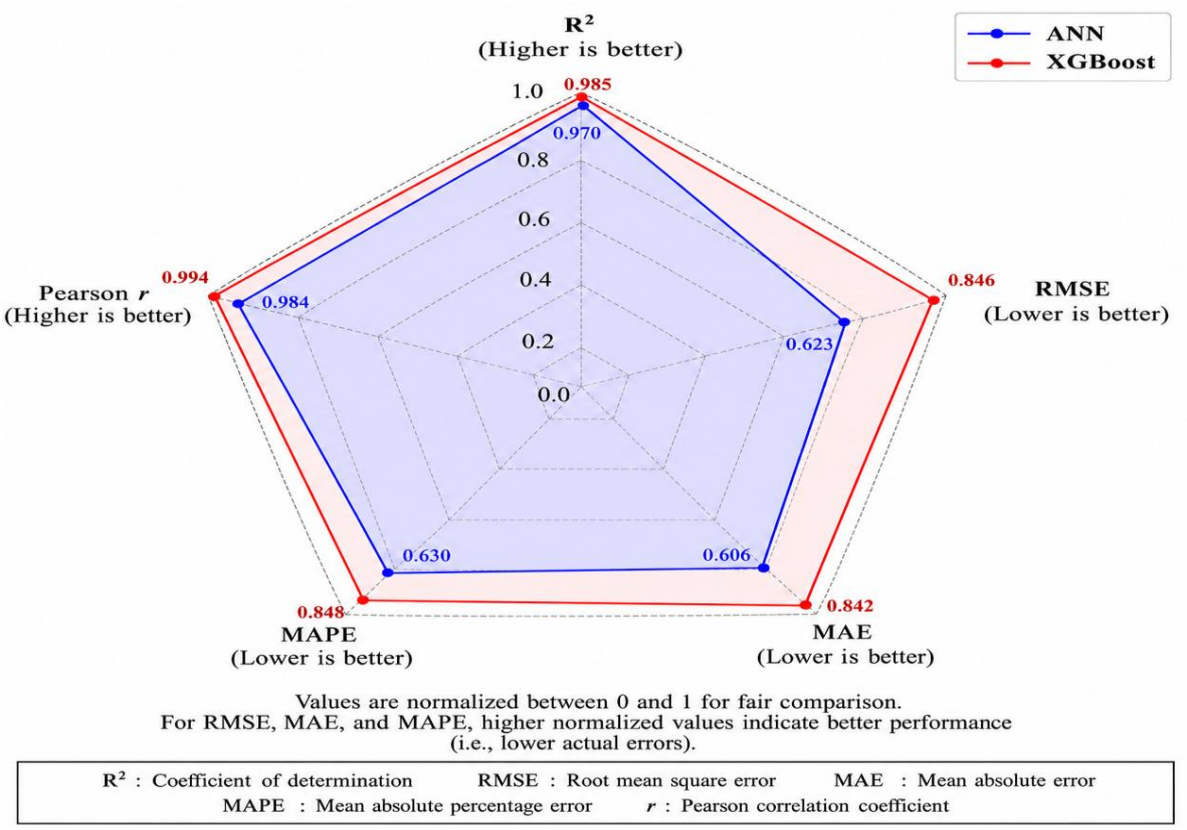

Figure 5. Radar chart illustrating the normalized predictive performance of the ANN and XGBoost models.

Figure 5 presents the normalized radar-chart comparison. The XGBoost profile remains above the ANN profile for the higher-is-better and lower-is-better metrics after normalization, consistent with the numerical results in Table 6. The stronger XGBoost performance is consistent with the way gradient boosting builds an ensemble of trees to capture nonlinear interactions while controlling model complexity through regularization [19]. In the present dataset, this approach produced lower prediction errors than the ANN model. From an engineering standpoint, the lower errors obtained with XGBoost improve the reliability of estimating both attenuation coefficients and derived shielding-thickness parameters. The model may therefore be useful for preliminary material screening and shielding-thickness assessment before extensive experimental testing.

4.3.2 Comparative Interpretation of ANN and XGBoost Models

The performance metrics establish how accurately the two models predict the shielding parameters, but they do not show how individual input features contribute to those predictions. SHAP [22,23] was therefore used to interpret the feature contributions of ANN and XGBoost. Figures 6 and 7 and Table 7 present the SHAP summary plots, global feature-importance rankings, and corresponding quantitative values.

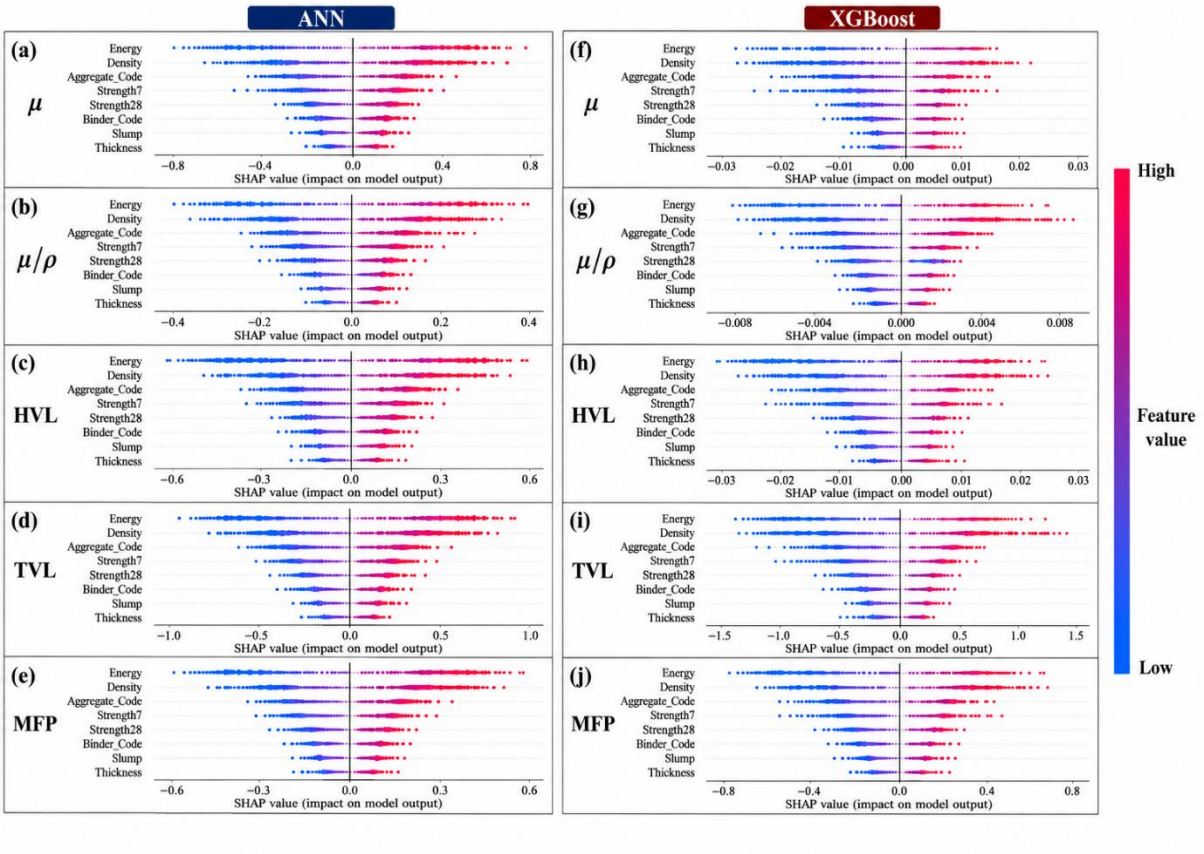

Figure 6. Comparative SHAP summary (beeswarm) plots of the ANN and XGBoost models for predicting (a) μ, (b) μ/ρ, (c) HVL, (d) TVL, and (e) MFP.

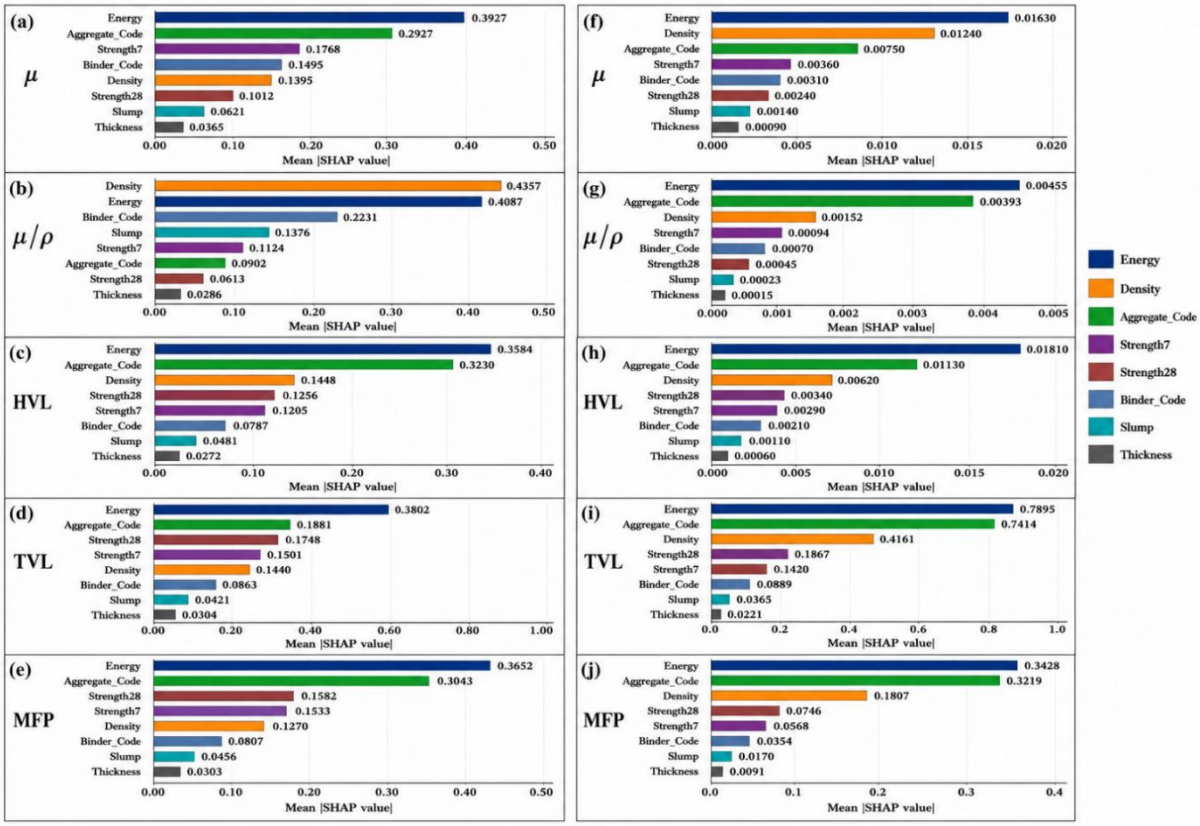

Figure 7. Comparative global SHAP feature importance (mean absolute SHAP values) of the ANN and XGBoost models.

Table 7. Comparative SHAP feature importance values and rankings of the ANN and XGBoost models for predicting gamma-ray shielding parameters.

Feature	μ (ANN)	μ (XGB)	μ/ρ (ANN)	μ/ρ (XGB)	HVL (ANN)	HVL (XGB)	TVL (ANN)	TVL (XGB)	MFP (ANN)	MFP (XGB)
Photon Energy	0.3927 (1)	0.0163 (1)	0.4087 (2)	0.00455 (1)	0.3584 (1)	0.0181 (1)	0.3802 (1)	0.7895 (1)	0.3652 (1)	0.3428 (1)
Density	0.1395 (5)	0.0124 (2)	0.4357 (1)	0.00152 (3)	0.1448 (3)	0.00620 (3)	0.1440 (5)	0.4161 (3)	0.1270 (5)	0.1807 (3)
Aggregate_ Code	0.2927 (2)	0.00750 (3)	0.0902 (6)	0.00393 (2)	0.3230 (2)	0.0113 (2)	0.1881 (2)	0.7414 (2)	0.3043 (2)	0.3219 (2)
Strength7	0.1768 (3)	0.00360 (4)	0.1124 (5)	0.00094 (4)	0.1205 (5)	0.00290 (5)	0.1501 (4)	0.1420 (5)	0.1533 (4)	0.0568 (5)
Strength28	0.1012 (6)	0.00240 (6)	0.0613 (7)	0.00045 (6)	0.1256 (4)	0.00340 (4)	0.1748 (3)	0.1867 (4)	0.1582 (3)	0.0746 (4)
Binder_Code	0.1495 (4)	0.00310 (5)	0.2231 (3)	0.00070 (5)	0.0787 (6)	0.00210 (6)	0.0863 (6)	0.0889 (6)	0.0807 (6)	0.0354 (6)
Slump	0.0621 (7)	0.00140 (7)	0.1376 (4)	0.00023 (7)	0.0481 (7)	0.00110 (7)	0.0421 (7)	0.0365 (7)	0.0456 (7)	0.0170 (7)
Thickness	0.0365 (8)	0.00090 (8)	0.0286 (8)	0.00015 (8)	0.0272 (8)	0.00060 (8)	0.0304 (8)	0.0221 (8)	0.0303 (8)	0.0091 (8)

SHAP magnitudes are model-specific because they depend on how each algorithm represents the relationship between inputs and outputs [22,23]. Although both models used the same eight numerical features, ANN learns through interconnected network weights, whereas XGBoost builds decision trees sequentially. ANN can therefore distribute contribution across several interacting variables, while XGBoost may concentrate contribution on features that most reduce prediction error. For this reason, absolute SHAP magnitudes are best compared within each model; feature rankings provide the more direct basis for cross-model interpretation.

Photon Energy was consistently ranked as the most influential feature for the five shielding parameters in both models. For μ, ANN assigned 0.3927 to Photon Energy, followed by Aggregate_Code (0.2927) and Strength7 (0.1768). XGBoost ranked Photon Energy (0.0163), Density (0.0124), and Aggregate_Code (0.00750) highest. Thus, the ANN importance profile was more distributed, whereas XGBoost placed greater emphasis on photon energy and the principal material-related variables.

For μ/ρ, Density was the leading ANN feature with a SHAP value of 0.4357, followed by Photon Energy (0.4087) and Binder_Code (0.2231). XGBoost ranked Photon Energy (0.00455) first, followed by Aggregate_Code (0.00393) and Density (0.00152). For HVL, Photon Energy remained the leading feature in both models, with SHAP values of 0.3584 for ANN and 0.0181 for XGBoost; Aggregate_Code was second in both cases. The rankings show that the two algorithms extracted different feature-use patterns from the same experimental information.

The difference was particularly clear for TVL. In XGBoost, Photon Energy (0.7895), Aggregate_Code (0.7414), and Density (0.4161) had the largest within-model SHAP contributions. ANN showed a broader distribution, led by Photon Energy (0.3802), Aggregate_Code (0.1881), Strength28 (0.1748), and Density (0.1440). For MFP, Photon Energy was again the leading feature and Aggregate_Code ranked second in both models, while ANN assigned relatively greater importance to Strength7 and Strength28. These patterns indicate that ANN retained broader associations with material and mechanical variables, whereas XGBoost emphasized the principal radiation-related inputs.

The SHAP interpretation is consistent with the predictive comparison. XGBoost reduced RMSE, MAE, and MAPE for μ by 36.76%, 35.52%, and 35.65%, respectively, and reduced the corresponding errors for μ/ρ by 25.84%, 26.46%, and 28.41%. For HVL, TVL, and MFP, the reductions were approximately 17–32%. The combination of lower prediction errors and the feature rankings therefore provides a consistent picture of XGBoost's behaviour on this dataset.

Taken together, the SHAP results show that both models recognized Photon Energy as a dominant predictor, with Aggregate_Code and Density among the principal material-related features. ANN distributed importance more widely across material and mechanical variables, whereas XGBoost concentrated more strongly on the dominant shielding-related inputs. This interpretation complements the statistical comparison and helps explain the different predictive behaviour of the two algorithms.

4.4 Engineering Implications

The proposed framework provides a data-driven means of estimating μ, μ/ρ, HVL, TVL, and MFP from experimentally measurable concrete and radiation variables. Because the models can produce predictions without repeating every attenuation experiment, they may be useful for preliminary screening and comparison of shielding materials. SHAP further identifies Photon Energy, Aggregate Code, and Density as influential predictors and provides a transparent view of how the models use the input variables. Within the present dataset, XGBoost produced the stronger predictive results and emphasized the principal attenuation-related features. These characteristics support its use for preliminary assessment and optimization of radiation-shielding concrete. The framework may be relevant to shielding concrete used in medical, industrial, and nuclear settings. Its broader applicability, however,

requires validation with larger and more diverse datasets covering additional concrete compositions, aggregate types, and radiation energies.

4.5 Limitations and Future Research

The present analysis is based on 216 experimental observations from six concrete mixtures and a limited range of aggregate types, photon energies, and specimen thicknesses. Although ANN and XGBoost achieved high predictive accuracy, these results should not be assumed to apply beyond the investigated material and radiation conditions without further validation. Future work should expand the database to include additional binder systems, aggregate types, concrete densities, and photon energies. Independent experiments and external datasets would also provide a stronger test of model generalization.

5. CONCLUSIONS

The major conclusions drawn from the present study are as follows:

- The investigated conventional and alkali-activated high-density concretes containing heavyweight aggregates showed strong gamma-ray shielding performance. The machine-learning models predicted μ, μ/ρ, HVL, TVL, and MFP from eight numerical predictor features derived from ten predictor-related variables, demonstrating the feasibility of the proposed data-driven approach for the investigated shielding concretes.
- Both ANN and XGBoost achieved high predictive accuracy, with XGBoost performing better for all five shielding parameters. For μ, R^2 increased from 0.9764 for ANN to 0.9906 for XGBoost. RMSE, MAE, and MAPE decreased from 0.00576 to 0.00364 cm^{-1}, from 0.00447 to 0.00288 cm^{-1}, and from 2.28% to 1.47%, respectively.
- The same trend was observed for the other outputs. For μ/ρ, R^2 increased from 0.9628 to 0.9796, with lower prediction errors for XGBoost. Across the five shielding parameters, XGBoost reduced prediction errors by approximately 17–36% relative to ANN, indicating stronger performance for the nonlinear relationships represented in this dataset.
- SHAP analysis identified Photon Energy as the dominant predictor across the five shielding parameters, while Aggregate Code and Density were among the most influential material-related variables. This pattern is consistent with the established role of photon energy and material characteristics in gamma-ray attenuation.
- The two algorithms also showed different feature-use patterns. ANN distributed predictive importance more broadly across strength- and binder-related variables, whereas XGBoost placed greater emphasis on Photon Energy, Aggregate Code, and Density.
- Overall, the XGBoost–SHAP framework provides an interpretable approach for predicting the investigated gamma-ray shielding parameters. Within the limits of the present database, it can support preliminary evaluation and design of high-density shielding concrete while reducing the need for extensive initial experimental screening.

Declarations

Corresponding Author:
Corresponding author: Divakar L
Email: divakarl.ce.et@msruas.ac.in

Funding:
This research received no external funding

Consent for Publication:
Not applicable

Conflict Of Interest:
The authors declare no conflict of interest.

Ethics Approval and Consent to Participate:
Not applicable

Author Contribution:
Divakar L: Conceptualization, Methodology, Literature review, Data curation, Formal analysis, Visualization, Writing – original draft.
Dr. Chethan Gowda R. K.: Conceptualization, Supervision, Validation, Project administration, Writing – review & editing.
S. D. Anitha Kumari: Supervision, Validation, Critical review, Writing – review & editing.
All authors have read and agreed to the published version of the manuscript.

REFERENCES

1. Barbhuiya, S., Das, B. B., Norman, P., & Qureshi, T. (2025). A comprehensive review of radiation shielding concrete: Properties, design, evaluation, and applications. Structural Concrete, 26(2), 1809–1855. https://doi.org/10.1002/suco.202400519
2. Onaizi, A. M., Amran, M., Tang, W., Betoush, N., Alhassan, M., Rashid, R. S. M., Yasin, M. F., Bayagoob, K. H., & Onaizi, S. A. (2024). Radiation-shielding concrete: A review of materials, performance, and the impact of radiation on concrete properties. Journal of Building Engineering, 97, 110800. https://doi.org/10.1016/j.jobe.2024.110800
3. Akkurt, I., Basyigit, C., Kilincarslan, S., & Mavi, B. (2005). The shielding of γ-rays by concretes produced with barite. Progress in Nuclear Energy, 46(1), 1–11. https://doi.org/10.1016/j.pnucene.2004.09.015
4. Akkurt, I., & El-Khayatt, A. M. (2013). The effect of barite proportion on neutron and gamma-ray shielding. Annals of Nuclear Energy, 51, 5–9. https://doi.org/10.1016/j.anucene.2012.08.026
5. Shams, T., Eftekhar, M., & Shirani, A. (2018). Investigation of gamma radiation attenuation in heavy concrete shields containing hematite and barite aggregates in multi-layered and mixed forms. Construction and Building Materials, 182, 35–42. https://doi.org/10.1016/j.conbuildmat.2018.06.032
6. Gunoglu, K., & Akkurt, İ. (2021). Radiation shielding properties of concrete containing magnetite. Progress in Nuclear Energy, 137, 103776. https://doi.org/10.1016/j.pnucene.2021.103776
7. Abdullah, M. A. H., Rashid, R. S. M., Amran, M., Hejazii, F., Azreen, N. M., Fediuk, R., Voo, Y. L., Vatin, N. I., & Idris, M. I. (2022). Recent trends in advanced radiation shielding concrete for construction of facilities: Materials and properties. Polymers, 14(14), 2830. https://doi.org/10.3390/polym14142830
8. Zhou, C., Guo, H.-Y., & Dai, J.-G. (2025). Data-driven investigation and multi-objective optimization design of alkali-activated concrete. Journal of Asian Concrete Federation, 11(1), 53–70. https://doi.org/10.18702/acf.2025.11.1.53
9. Ali, A. Y. F., Ahmed, S. A., & El-Feky, M. A. (2025). Alkali-activated concrete with expanded polystyrene: A lightweight, high-strength solution for fire resistance and explosive protection. Journal of Building Engineering, 99, 111648. https://doi.org/10.1016/j.jobe.2024.111648
10. Vargas, J. F., Oviedo, A. I., Ortega, N. A., Orozco, E., Gómez, A., & Londoño, J. M. (2024). Machine-learning-based predictive models for compressive strength, flexural strength, and slump of concrete. Applied Sciences, 14(11), 4426. https://doi.org/10.3390/app14114426
11. Liu, Y. (2022). High-performance concrete strength prediction based on machine learning. Computational Intelligence and Neuroscience, 2022, Article 5802217. https://doi.org/10.1155/2022/5802217
12. El-Sayed, A. A., Fathy, I. N., Tayeh, B. A., & Almeshal, I. (2022). Using artificial neural networks for predicting mechanical and radiation shielding properties of different nano-concretes exposed to elevated temperature. Construction and Building Materials, 324, 126663. https://doi.org/10.1016/j.conbuildmat.2022.126663
13. Chen, T., & Guestrin, C. (2016). XGBoost: A scalable tree boosting system. In Proceedings of the 22nd ACM SIGKDD International Conference on Knowledge Discovery and Data Mining (pp. 785–794). https://doi.org/10.1145/2939672.2939785

14. Amin, M. N., Ahmad, I., Iqbal, M., Abbas, A., Khan, K., Faraz, M. I., Alabdullah, A. A., & Ullah, S. (2022). Computational AI models for investigating the radiation shielding potential of high-density concrete. Materials, 15(13), 4573. https://doi.org/10.3390/ma15134573
15. Nahool, T. A., Abdelmonem, A. M., Ali, M. S., & Yasser, A. M. (2024). Using machine learning to predict gamma shielding properties: A comparative study. New Journal of Physics, 26(9), 093035. https://doi.org/10.1088/1367-2630/ad4a21
16. Alkharisi, M. K., Dahish, H. A., & Youssf, O. (2024). Prediction models for the hybrid effect of nano materials on radiation shielding properties of concrete exposed to elevated temperatures. Case Studies in Construction Materials, 21, e03750. https://doi.org/10.1016/j.cscm.2024.e03750
17. El-Sawy, A. A., & Sarwat, E. (2024). Comparative study of gamma-ray shielding parameters for different epoxy composites using ANN, MCNP-5 and WinXCOM. Baghdad Science Journal, 21(2), Article 4. https://doi.org/10.21123/bsj.2023.7685
18. Amin, M. N., Ahmad, I., Abbas, A., Khan, K., Qadir, M. G., Iqbal, M., Abu-Arab, A. M., & Alabdullah, A. A. (2022). Estimating radiation shielding of fired clay bricks using ANN and GEP approaches. Materials, 15(17), 5908. https://doi.org/10.3390/ma15175908
19. Mahmoud, A. A., El-Sayed, A. A., Aboraya, A. M., Fathy, I. N., & Nabil, I. M. (2025). Enhancing predictive accuracy of nano-additive concrete gamma ray attenuation at high temperatures using AI-based models. Neural Computing and Applications, 37(26), 21833–21866. https://doi.org/10.1007/s00521-025-11491-0
20. Li, Y., Wang, G., Amin, M. N., Iftikhar, B., & Ahmad, A. (2024). Fresh state and strength performance evaluation of slag-based alkali-activated concrete using soft-computing methods. Materials Today Communications, 38, 107822. https://doi.org/10.1016/j.mtcomm.2023.107822
21. Saxena, S., & Sharma, H. (2025). Prediction and assessment of optimal concrete compositions for overall radiation protection and reduced global warming potential. Scientific Reports, 15, 5785. https://doi.org/10.1038/s41598-025-89683-w
22. Lundberg, S. M., & Lee, S.-I. (2017). A unified approach to interpreting model predictions. Advances in Neural Information Processing Systems, 30, 4765–4774. https://proceedings.neurips.cc/paper_files/paper/2017/hash/8a20a8621978632d76c43dfd28b67767-Abstract.html
23. Taffese, W. Z., & Espinosa-Leal, L. (2024). Unveiling non-steady chloride migration insights through explainable machine learning. Journal of Building Engineering, 82, 108370. https://doi.org/10.1016/j.jobe.2023.108370
24. Kalauni, K., Czirak, P., Chaturvedi, S., Palou, M. T., & Vedrtnam, A. (2025). Performance and design considerations for heavyweight self-compacting concrete using magnetite and barite aggregates. Journal of Building Engineering, 111, 113626. https://doi.org/10.1016/j.jobe.2025.113626
25. Awadeen, M., Amin, M., Bakr, R. H., & Tahwia, A. M. (2024). Mechanical properties, attenuation coefficient, and microstructure of ultra high-performance heavyweight concrete for radiation shielding applications. Journal of Building Engineering, 82, 108395. https://doi.org/10.1016/j.jobe.2023.108395
26. Anunike, G. S., Tarabin, M., & Hisseine, O. A. (2024). Ultra-high-performance concrete for nuclear applications: A review of raw materials and mix design approaches.

Construction and Building Materials, 438, 136938. https://doi.org/10.1016/j.conbuildmat.2024.136938

27. Wahab, S., Khan, I. U., Khan, M. N. A., & Ashraf, M. (2024). Development and evaluation of MgO-grit iron aggregate heavy density concrete for high temperature radiation shielding: Experimental and machine learning approach. Construction and Building Materials, 439, 137381. https://doi.org/10.1016/j.conbuildmat.2024.137381

28. Kang, Y., & Zu, J. (2026). Gamma-ray buildup factor calculation via an automated machine learning framework with integrated analysis. Annals of Nuclear Energy, 227, 111971. https://doi.org/10.1016/j.anucene.2025.111971